

Context-self contrastive pretraining for crop type semantic segmentation

Michail Tarasiou
Imperial College London

Rıza Alp Güler
Imperial College London

Stefanos Zafeiriou
Imperial College London

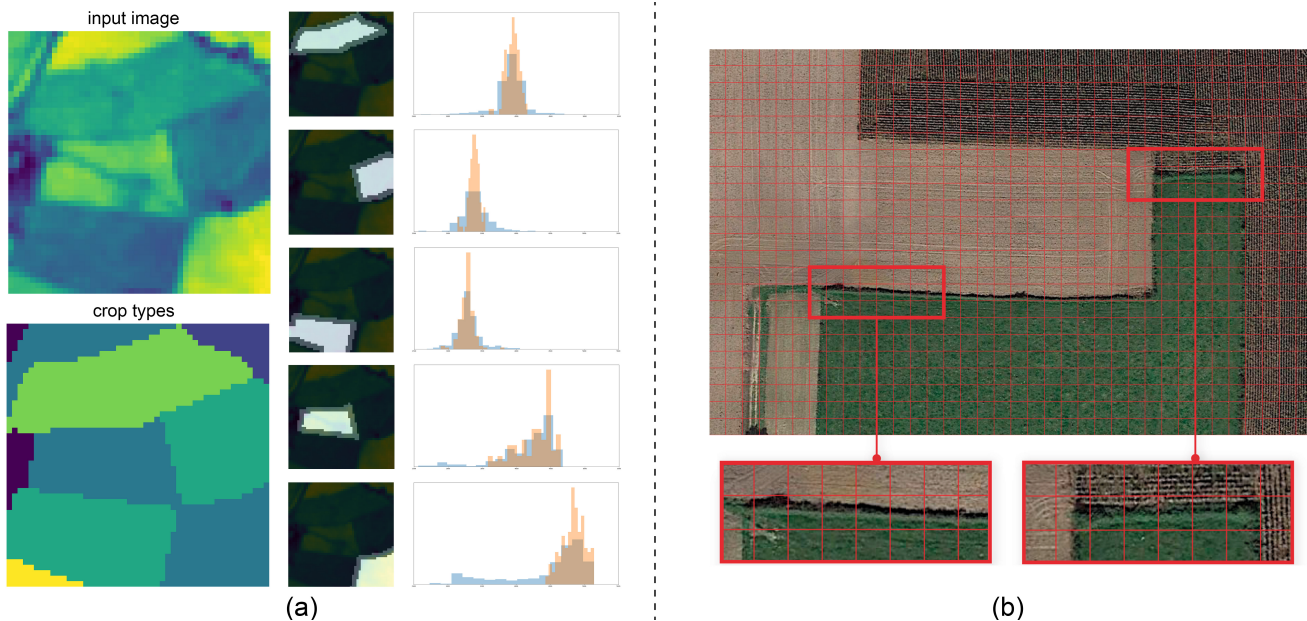


Figure 1: (a) In satellite images interior regions of agricultural fields consist of large homogeneous regions with little signal variation as shown in histograms of intensities over whole parcel regions (blue) and interior points (orange). (b) Pixel size is coarse enough for the signal at boundaries to mix. Here the 10m resolution *Sentinel-2* grid is overlaid on a high-resolution image from *Google Earth*. The magnified regions show grid locations that contain signal from multiple crop types and objects. The proposed *Context-Self Contrastive Loss* directly compares computed embeddings in local neighbourhoods. As such, interior regions naturally have a small contribution to the overall loss while at the same time the network learns to disambiguate boundary pixels by comparing them to nearby locations.

Abstract

In this paper we propose a fully-supervised pretraining scheme based on contrastive learning particularly tailored to dense classification tasks. The proposed *Context-Self Contrastive Loss (CSCL)* learns an embedding space that makes semantic boundaries pop-up by use of a similarity metric between every location in an training sample and its local context. For crop type semantic segmentation from satellite images we find performance at parcel boundaries to be a critical bottleneck and explain how CSCL tackles the underlying cause of that problem, improving the state-of-

the-art performance in this task. Additionally, using images from the *Sentinel-2 (S2)* satellite missions we compile the largest, to our knowledge, dataset of satellite image time-series densely annotated by crop type and parcel identities, which we make publicly available together with the data generation pipeline. Using that data we find CSCL, even with minimal pretraining, to improve all respective baselines and present a process for semantic segmentation at super-resolution for obtaining crop classes at a more granular level. The proposed method is further validated on the task of semantic segmentation on 2D and 3D volumetric images showing consistent performance improvements upon competitive baselines.

⁰Imagery ©2020 Google, Imagery ©Maxar Technologies, Map data ©2020, Imagery Date: 10/11/2017.

1. Introduction

The large availability of imagery made available by *Earth Observation* (EO) satellites has enabled the development of tools for the automated monitoring of food supplies and the design and control of policies aiming at agricultural development. In the *European Union* (EU) agricultural subsidies provided as part of the *Common Agricultural Policy* (CAP) comprised approximately 39% of last year’s overall budget at €59 billion. Distribution of these subsidies to over 10 million farms is currently performed by use of crop maps which are compiled by parcel topographies and crop types declared by EU farmers. New reforms of the CAP are expected to place particular emphasis on the use of automated tools for EO. In particular, the *Sentinels for Common Agricultural Policy* (Sen4CAP) project aims at making use of the *European Space Agency* (ESA) *Sentinel* satellites for providing stakeholders with validated algorithms, products and tools relevant for the management of the CAP. Provided examples for CAP monitoring of agricultural practices¹ and crop diversification requirements² both impose thresholds on the area of declared arable land dedicated to different crop types. Their accuracy should benefit greatly from the development of automated crop identification processes at high granularity.

However, a performance analysis of state-of-the-art large-scale crop-type identification systems presented in section 5.2 showed us that the classification accuracy varies with the location within a parcel and drops significantly near the parcel boundaries. While this is in part expected for all dense labelling tasks we attribute the additional difficulty of correctly classifying parcel boundaries to the fact that satellites dedicated to monitoring land surface variability trade off resolution with high revisit time. As a result pixel size is coarse enough for the signal from different crop types or objects to mix. This is demonstrated in Fig.1 (b), where we overlay the resolution at hand on high resolution images. The highest resolution band of *S2* images covers a 10×10m region per pixel. Note that this pixel-size is large enough to include complete objects such as roads, which adds further complexity to the problem. For crop classification at the parcel level [15] argue that this pixel size is coarser than the typical agricultural textural information and show that using spatial modelling is not at all critical for good performance. What would be the best strategy though if we are interested in predicting crop types for every pixel and moreover for boundary pixels which are the most severely affected by the coarse size? We argue that class attribution near boundaries can be improved by learning to detect semantic boundaries by contrasting each pixel with their neighbourhood pixels. Furthermore, interior locations of agricultural parcels

¹<http://esa-sen4cap.org/content/agricultural-practices>

²<http://esa-sen4cap.org/content/crop-diversification>

in satellite images include large homogeneous regions with little structure and small signal variation as shown Fig.1(a). While the *Cross-Entropy* (CE) criterion still needs to assign a class to all interior pixels a contrastive criterion constrained to local neighbourhoods naturally contains a small loss contribution from these regions as they are encoded by similar embeddings. The above two observations constitute the motivation behind our proposed method. Our key contributions are the following:

1. Inspired by recent developments on visual self-attention we design a metric learning pretrain scheme, targeting performance at the parcel boundaries (section 3). Applying the proposed approach on a publicly available crop segmentation dataset, we raise the state-of-the-art *mIoU* from 78.03% to 81.12% (section 5.1). Furthermore, we show the generality of our method on semantic segmentation of 2D and 3D images by improving upon baselines (section 5.5).
2. Regional variations of plant growth patterns is a major challenge hindering generalization. We present the largest, measured by *Area of Interest* (AOI), *Time Period of Interest* (POI) and number of crop types, dataset for crop type segmentation which we make publicly available together with the data generation pipeline in an effort to facilitate future research (section 4.1). To our knowledge this is also the first dataset to include dense annotations for parcel identities and labels at super-resolution. We benchmark this dataset with state-of-the-art models which we consistently outperform using our pretraining scheme (section 5.1).
3. We present a simple method for segmenting crops from satellite images at a higher resolution than the input by leveraging available ground truths and show performance improvements in segmenting crops at ×4 the input resolution over training at base resolution (section 5.4).

2. Related work

Crop type identification from satellite images is a challenging task that involves assigning one of C crop categories at a set of desired locations on a geospatial grid, most commonly at the agricultural parcel or pixel level. Rather than using single images as inputs crop identification has been shown to work best by modelling of the temporal patterns of plant growth during a growing season. *Remote Sensing* approaches have traditionally used multiple preprocessing steps, adding expert knowledge to correct satellite image capturing and extract hand-crafted features, e.g. various vegetation indices [20] used as input to machine learning classifiers [11, 31, 17, 10, 40, 29]. More recently *DNNs* have achieved increasingly competitive per-

formance outperforming previous approaches by a large margin. These methods make use of minimal data preprocessing and are shown to handle challenges such as cloudy images, image noise and atmospheric corrections automatically during network feature extraction [36, 34, 37]. Some works involve temporal modelling of single pixel or parcel level aggregated features [35, 30, 15] while others jointly capture temporal and spatial patterns [36, 19, 34, 14]. Fewer works have tackled semantic segmentation of crop types [36, 34]. In particular [34] propose two types of models: a fully convolutional *3D-UNET* [9] and a *2D-UNET* feature extractor coupled with a *CLSTM* decoder [39] both achieving state-of-the-art performance. In our work we use a novel contrastive pre-training scheme to significantly improve these results. On super-resolution with satellite images [25] present a method for semantic segmentation at the resolution of input images utilizing only low-resolution ground-truth labels and assuming a known joint distribution between low and high-resolution ground truths. Our method utilizes vector representations of parcel geometries which are a common output of agricultural field studies and makes no further assumptions. It is also different in that we predict classes at a higher resolution than inputs.

Metric learning aims at estimating the similarity between samples by use of a distance metric. In a fully supervised setting known labels are used to gather pairs of positive (similar) and negative (dissimilar) samples and a model is trained such that positive pairs are brought closer in embedding space while negative pairs are contrasted. The seminal work of [8] for the face verification task used a *Siamese Neural Network* [5] architecture to process two input samples with known semantic similarity. Since then several works employed contrastive learning to enhance the discriminatory capacity of neural networks in downstream classification tasks. This can be achieved by either learning a linear classifier directly on the latent space [46, 42, 6, 18, 7, 28], or by using network weights as a good initialization point for further end-to-end training [45, 41]. In terms of supervision [46, 42, 6, 18, 28, 45] use instance discrimination coupled with strong data augmentation as a self-supervision pretext task while [16, 38, 23, 22] use available annotations to drive sample similarities in a fully supervised setting. [28, 45] both use self-supervision to improve performance on dense classification. Our method is a fully supervised metric learning scheme specifically designed for dense classification tasks. Also in contrast to other approaches we draw both positive and negative pairs from the same sample using a single model pass and do not require the use of large batch size or data queues.

Self-attention was introduced in [43] for the 1D task of machine translation and involves learning useful similarities between features at different positions which are later used to derive weights for averaging them. For vision tasks

[44] propose using self-attention as an additional permutation equivariant layer to *CNN* architectures and [4] introduced the use of two dimensional relative positional embeddings to remove the permutation equivariance property while remaining translation equivariant. Both works attend over a global receptive field which scales $\mathcal{O}(H^2W^2)$ with the input size $(H \times W)$ and are thus prohibitive for high resolution inputs. More related to our method [32] restrict the receptive field of the self-attention module to a local $(h \times w)$ region, reduce the complexity to $\mathcal{O}(HWhw)$ and use this module as stand-alone primitive in place convolution layers to construct deep architectures. Our method, inspired by this approach, calculates a local affinity matrix of final layer embeddings but rather than using it for feature aggregation we apply supervision directly on calculated affinities.

3. Context-Self Contrastive pretraining

Applied on an N -dimensional embedding space of a *CNN*, the affinity matrix of a self-attention layer naturally encodes semantic similarity between features extracted at different locations. Using densely annotated data, we derive class agnostic labels for providing full supervision on the values of the similarity matrix and train a network on the task of predicting class agreement between each location paired with all locations in its local neighbourhood. The trained network is later used as an initialization point for end-to-end training on a dense classification task. In its most general form, the proposed methodology includes the following components:

1. an encoder function $y = f(x)$ mapping an input tensor x to an output feature map y
2. a similarity function $s = g(y)$
3. a ground truth generator $l_s = r(l)$ generating class-agnostic ground truths l_s from dense annotations l
4. a decoder $o = h(y)$ mapping encoded features to the desired output
5. two loss functions $L_{pretrain}(s, l_s)$ and $L_{train}(o, l)$

In this paper, the encoder function is a deep *CNN*, the decoder is a simple linear layer $o = W_{dy}$ ³, y , l and o are N -dimensional tensors while s and l_s have $2N$ spatial dimensions. In the following, we describe individual components for $N = 2$ without loss of generality.

3.1. Ground truth generator

For ground truths $l \in \{0, 1\}^{H \times W \times C}$, $\sum_k l_{ijk} = 1$, where C is the number of classes, we obtain suitable labels

³we have found the use of more sophisticated decoders to offer small performance gains over a linear decoder

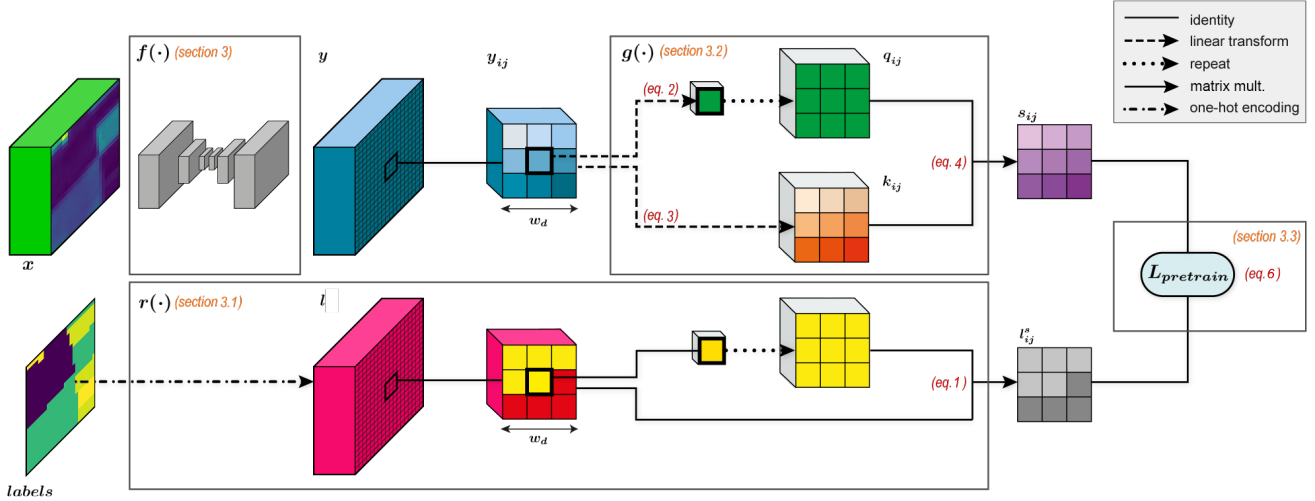


Figure 2: Proposed pretraining scheme using the *Context-Self Contrastive Loss (CSCL)*. For a CNN feature map y we define a similarity metric s_{ij} between features extracted at all locations (i, j) and every location in their w_d -neighbourhood (top branch). Similarly, we derive training labels l^s from dense annotations l for fully supervised training (bottom branch).

that encode class agreement between each location (i, j) and its $(w_d \times w_d)$, w_r -dilated neighbourhood by application of the element-wise dot-product.

$$l_{ij}^s = l_{ij}^T l_{\mathcal{N}_{w_d, w_r}(ij)} \in \{0, 1\}^{w_d \times w_d} \quad (1)$$

Here $\mathcal{N}_{w_d, w_r}(ij)$ denotes the $(w_d \times w_d)$, w_r -dilated neighbourhood centered around location (i, j) . We note the option of applying eq.(4) at a stride w_s to reduce the amount of computation in high resolution outputs leading to a ground-truth tensor of dimensions $(\frac{H}{w_s} \times \frac{W}{w_s} \times w_d \times w_d)$. The process is shown at the bottom branch of Fig.2 while an example of generated labels for various size and dilation parameters is shown in Fig.3. In order to mask supervision at the zero-padded regions and at the centers of extracted windows we use a mask tensor $m \in \{0, 1\}^{\frac{H}{w_s} \times \frac{W}{w_s} \times w_d \times w_d}$.

3.2. Similarity function

Drawing inspiration from [32] we use a local affinity matrix as our similarity metric. Formally for a feature map $y \in \mathbb{R}^{H \times W \times D}$ we calculate *queries* and *keys* tensors

$$q_{ij} = W_q y_{ij} \in \mathbb{R}^{D_1} \quad (2)$$

$$k_{ij} = W_k y_{ij} \in \mathbb{R}^{D_1} \quad (3)$$

Where $W_q, W_k \in \mathbb{R}^{D_1 \times D}$. We augment the *keys* with positional embeddings similar to [4] and calculate the similarity tensor s by applying the element-wise dot-product over unit-sphere normalized *queries* and local *keys*

$$s_{ij} = \hat{q}_{ij}^T \hat{k}_{\mathcal{N}_{w_d, w_r}(ij)} \in \mathbb{R}^{w_d \times w_d} \quad (4)$$

The process is shown at the top branch of Fig.2.

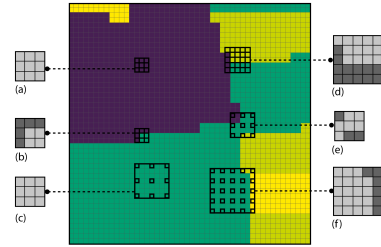


Figure 3: CSCL ground truth generator example on a 2D crop type label map. To generate labels we compare the class at the center location with all locations in the defined neighbourhood. We use windows with parameters (a, b) $w_d = 3, w_r = 1$, (c) $w_d = 3, w_r = 3$, (d) $w_d = 5, w_r = 1$, (e) $w_d = 3, w_r = 2$, (f) $w_d = 5, w_r = 2$.

3.3. Loss function

For $L_{pretrain}$ we use a contrastive loss function extending [16] to a dense embedding space and using cosine similarities of q and k instead of euclidean distances.

$$L_{pretrain} = -\frac{1}{\sum m} \sum (m \odot (l_s \odot s + (1 - l_s) \odot \max(0, margin - s))) \quad (5)$$

A number of studies has highlighted the importance of hard negative pairs in contrastive learning [16, 21, 33]. In our method all negative pairs originate from nearby locations in the same sample featuring high overlaps in their receptive fields. As such there is no possibility for easy negatives and we can discard the *margin* parameter originally employed to exclude the contribution of these pairs. For all our experiments we set $margin = 1$ and weight the contribution

of positive pairs by λ leading to the following equivalent expression.

$$L_{pretrain} = -\frac{1}{\sum m} \sum (m \odot ((\lambda + 1)l_s - 1) \odot s) \quad (6)$$

3.4. Interpreting the sliding window parameters

We note two ways in which the values of the sliding window parameters w_d , w_r affect training. First, they introduce a trade-off between the difficulty of fitting positive and negative pairs. Small w_d , w_r values results in comparing locations which are closer together making it easier to recognise positive pairs and harder for negative pairs, the other way being the case for large window size and dilation values. Secondly, they affect the statistics of the generated labels. Small w_d , w_r values results in comparing locations which are closer together and are more likely to belong to the same object resulting in a higher proportion of positive pairs. Class imbalance in class-agnostic ground truths - in favour of positive pairs - has been identified as a key issue. This effect is more pronounced for high resolution outputs, in which case we have found it beneficial to increase w_d , w_r and reduce λ . Choosing $w_s > 1$ can be used to reduce *CSCL* memory requirements. We note that for some values of $w_r > 1$, $w_s > 1$ some locations (i, j) are never used for calculating s , facilitating a more efficient implementation. This is further elaborated in the supplementary material.

4. Crop type segmentation

4.1. New dataset for crop type segmentation

For generating our densely annotated crop type segmentation dataset we are using ground truth crop type data available in the records of the *French Land Parcel Identification System* (RPG) ⁴ in the form of parcel geometries. As a source of satellite images we use *S2* products available through the *Copernicus Open Access Hub* (COAH) ⁵.

The automated process for generating the dataset includes the following steps: defining an AOI and a POI, downloading all relevant satellite images, extracting and rasterizing all relevant ground truth data, grouping and sorting satellite images to create timeseries objects and matching ground truths with timeseries by location. As a final step we create *boolean* masks for regions that should be masked out during training and inference. These include non-agricultural regions, crop types we do not wish to include as well as pixels contained to more than one parcels due to geocoding errors. The new dataset covers the *T31TFM S2* tile in France. This is the same AOI as [15], however, we extend the time period of interest to three years (2016-18) and

⁴<https://www.data.gouv.fr/en/datasets/registre-parcellaire-graphique-rpg-contours-des-parcelles-et-ilots-cultureux-et-leur-groupe-de-cultures-majoritaire>. In total the RGP includes approximately 10M parcels

⁵<https://scihub.copernicus.eu/>

provide dense annotations for crop types and parcel identities. We split inputs and ground truths into 480m square regions corresponding to 48×48 pixels for the highest resolution satellite band. During the ground truth rasterization step we also construct ground truths at $\times 4$ super-resolution corresponding to a 2.5m grid. Our dataset is the largest, to our knowledge, publicly available dataset for crop type semantic segmentation. Its AOI covers a full densely cultivated *S2* tile and by including 3 years it spans the longest time period among similar datasets. Additionally, this is the first dataset to include semantic labels at a higher resolution than input images and the first to enable training of parcel instance segmentation. In Table 1 we compare our dataset with other large scale crop type identification datasets. Data sample plots and further statistics are included in the supplementary material. To facilitate further research, we plan to make this dataset publicly available together with the data generation pipeline and evaluation codes.

4.2. Network architectures

All models explored here learn a mapping from image timeseries to a dense label map, i.e. $f : \mathbb{R}^{T \times H \times W \times D} \rightarrow \mathbb{R}^{H \times W \times C}$ where D equals the number of bands in a multispectral satellite image plus a *day* (day of year) parameter and C is the number of crop types. An additional *background* class is used to indicate areas not characterized by one of the C classes.

In the experiments that follow we use the backbone architectures from [34]. We have modified the *UNET3D* model [9] to make it more suitable to metric learning by increasing the capacity of the final layers and adding an extra layer in order to extract 128-dimensional embeddings. From here on we refer to the new model as *UNET3Df*. For the super-resolution experiments we process y using two 2D upsampling blocks each consisting of a transpose convolution layer with stride 2. For *CSCL* pretraining we use the final, size 128, 2D feature map as y . Details for all employed architectures are provided in the supplementary material.

5. Results

We split our France dataset into a train and evaluation set consisting of 120,438 and 18,749 samples respectively with no overlapping locations. We do not apply any label grouping but rather select classes directly from the 349 RPG codes such that there are at least 20,000 such parcels in the train set and 2,000 in the evaluation set for each year resulting in $C = 20$ classes in total. From publicly available crop segmentation datasets we make use of the dataset presented in [36] which covers an AOI of $102km \times 42km$ north of Munich, Germany containing $C = 17$ classes. We train all models using the provided train split and report results for the evaluation split for a fair comparison with literature.

country	A_{AOI} (ha)	N_{parc}	N_{years}	N_{bands}	N_T	CC_{max}	N_{cl}	dense annt.	ids annt.	SR labels
Romania [13]	64k	2.5k	1	4	13	10%	4	✗	✗	✗
France [15]	1.21M	200k	1	10	24	-	20	✗	✗	✗
Germany [36]	428k	137k	2	14	2-51	80%	17	✓	✗	✗
France (ours)	1.21M	200k	3	14	14-33	70%	166	✓	✓	✓

Table 1: Large scale datasets of satellite image timeseries for crop type recognition. A_{AOI} : AOI size in *hectares*, N_{parc} : number of parcels in AOI, N_{years} : number of growing seasons in dataset, N_{bands} : number of satellite image bands, N_T : number of observations for each growing season, CC_{max} : *maximum* cloud coverage, N_{cl} : number of crop types, *dense annt.*: dense annotations included, *ids annt.*: parcel ids included, *SR labels*: labels at super-resolution included.

For all experiments we use the *Adam* optimizer [24] with initial learn rate 0.0001, learn rate decay 0.975 applied at every epoch, beta parameters (0.9, 0.999) and batch size 32. All models are trained for 50 epochs for France and 150 epochs for Germany. For pretraining we use a sliding window with $w_d=3$, $w_r=1$, $w_s=1$ and $\lambda=0.125$. For the ablation studies we use the *UNET3Df* mainly because it is faster to train compared to *UNET2D-CLSTM*. We report *overall accuracy* and *mIoU*, *macro F1* scores in the *evaluation set*.

model	Acc.	mIoU	F1
BiCGRU [36]	0.897	-	0.831
UNET3D [34]	0.924	0.769	0.856
UNET2D-CLSTM [34]	0.927	0.780	0.868
UNET2D-CLSTM-CSCL	0.941	0.811	0.889
UNET3Df	0.926	0.772	0.859
UNET3Df-CSCL	0.938	0.799	0.878
UNET3D [34]	0.881	0.572	0.688
UNET2D-CLSTM [34]	0.888	0.581	0.687
UNET2D-CLSTM-CSCL	0.898	0.601	0.711
UNET3Df	0.886	0.571	0.685
UNET3Df-CSCL	0.892	0.599	0.702

Table 2: Model comparison for Germany (top) and France (bottom). Models from [34] were reimplemented using provided code as reported results used a custom evaluation set. A significant improvement over the baselines is achieved through CSCL pretraining using no additional data.

5.1. Comparison with state-of-the-art

We compare our method with recently proposed models in the datasets for Germany and France. Table 2 presents performance metrics and Fig.5 visually compares predictions, both indicating a clear advantage of *CSCL* over the randomly initialized baselines achieving new state-of-the-art results. We note that performance is significantly lower for France. This is mainly attributed to a few bad performing classes as explained in the supplementary material. As a sanity check we run further tests with the label groupings from [15] who reported *overall accuracy* 0.942 and *mIoU*

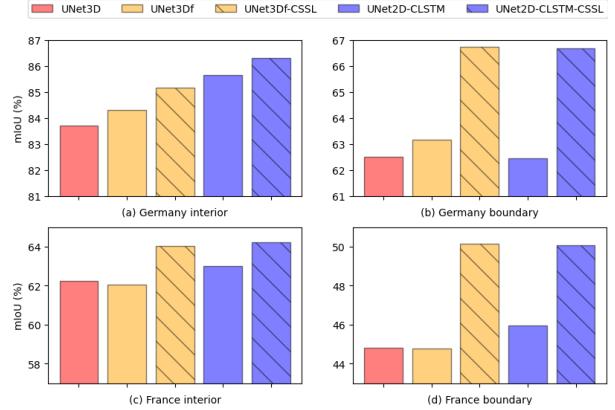


Figure 4: Model performance at parcel interior vs boundary locations. We demonstrate that the boost in segmentation performance mostly occurs near the parcel boundaries.

0.509 reaching similar performance (0.963 and 0.543) and although not comparable it indicates the added difficulty of training in this AOI.

5.2. Performance at parcel boundaries

For our analysis we define a semantic boundary as any location for which not all ground truths in a 3×3 local neighbourhood share the same value. By plotting model performance in terms of interior and boundary locations in Fig.4 we notice a clear performance drop at boundaries also evidenced by qualitative analysis of results in Fig.5. We also note that all models seem to have similar performance at interior locations, however, using *CSCL* there is a significant improvement at boundaries over the baselines showcasing the desired effect of the method.

5.3. Ablation of CSCL parameters

We present an ablation study on *CSCL* hyperparameters using our dataset in France for 2018. We find that the method is robust to varying parameters as we improve upon the no-pretraining baseline ($mIoU=0.532$) even when initializing with a model pretrained for only 1 epoch ($2k$ steps in Fig.6). Overall the ablations indicate the significance of negative pairs in achieving good performance.

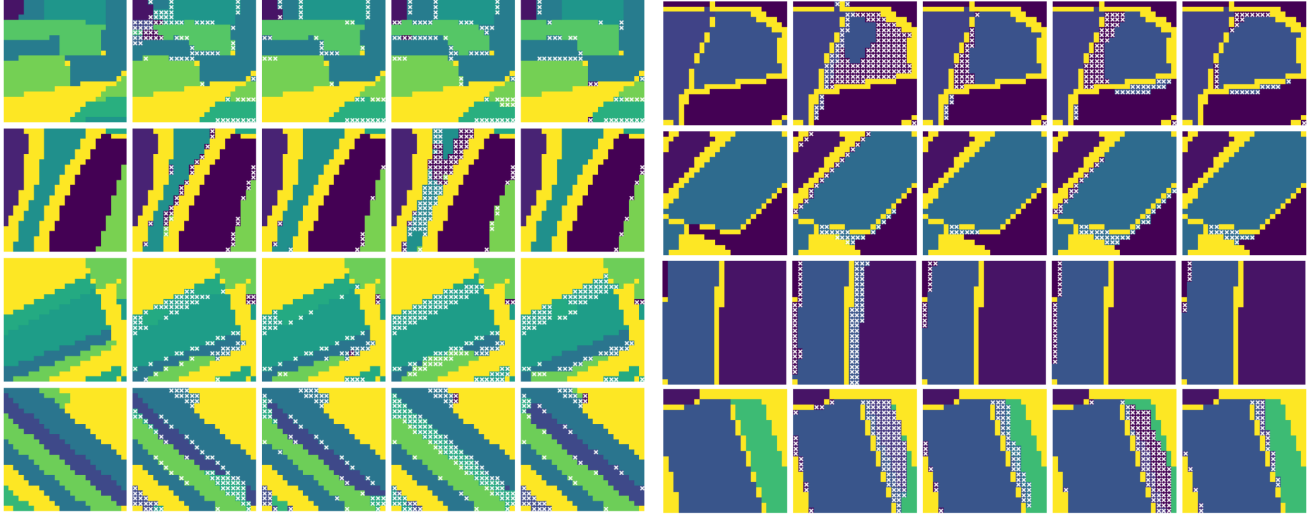


Figure 5: Qualitative comparison of models in Germany (left) and France (right). Left to right: ground truth labels, *UNET3Df*, *UNET3Df-CSCL*, *UNET2D-CLSTM*, *UNET2D-CLSTM-CSCL*. White "x" indicates false prediction at a particular location.

λ	0.01	0.05	0.125	0.25	0.50	1.0
mIoU	0.551	0.556	0.567	0.545	0.541	0.534

Table 3: Model *mIoU* from varying the weight λ of loss contribution from positive pairs.

$w_r \backslash w_d$	3	5	7
1	0.567 (3)	0.553 (5)	0.550 (7)
2	0.552 (5)	0.541 (9)	0.536 (13)

Table 4: Model *mIoU* for different *CSCL* window parameters. Corresponding w_d^{eff} in parenthesis.

In Table 3 we compare results varying the weight of loss from positive pairs λ finding that smaller weights lead to better performance. The ratio of negative to positive pairs in our training set is 0.111. The relationship between pre-training performance and final segmentation performance is examined in Fig. 6. This is done by sampling initializations from various pre-training steps. We demonstrate that lower loss and more heavily contrasted negative pairs during pre-training lead to better final performance. There appears to be no clear relationship between the mean cosine similarity for positive pairs and final performance. Results for varying *CSCL* window parameters are presented in Table 4. We find that windows covering smaller effective receptive fields ($w_d^{eff} = (w_d - 1) * w_r + 1$), thus containing harder negative pairs on average, perform better overall.

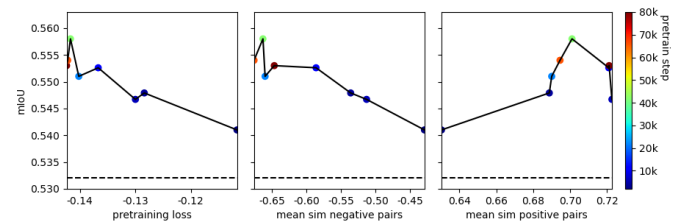


Figure 6: Model *mIoU* w.r.t. pretraining performance. Dashed line shows no-pretraining baseline, colormap indicates number of pretraining steps. A direct relationship is observed between pretraining quality and final performance.

model	train res.	Acc.	mIoU	F1
UNET3Df	$\times 4$	0.663	0.580	0.690
UNET3Df-CSCL	$\times 1$	0.668	0.587	0.698
UNET3Df-CSCL	$\times 4$	0.679	0.598	0.710

Table 5: Super-resolution model performance. The output of models trained at base ($\times 1$) resolution is upsampled to match $\times 4$ ground truths via nearest neighbour interpolation.

5.4. Semantic segmentation at super-resolution

In Table 5 we present results for the baseline and *CSCL* pretrained models using the $\times 4$ ground truths. To show the benefit over training with $\times 4$ ground truths we up-scale the output of the best model from Table 2 (train res. $\times 1$) via nearest neighbour interpolation. We note that $\times 4$ training outperforms the upsampled model (*mIoU* 0.598 vs 0.587) and that *CSCL* pretraining has a more significant effect that training at $\times 4$ resolution (*mIoU* 0.587 vs 0.580).



Figure 7: Qualitative comparison of super-resolution models from Table 5. From left to right: $UNet3Df-\times 4$, $UNet3Df-CSCL-\times 1$, $UNet3Df-CSCL-\times 4$. White "x" indicates false prediction at a particular location.

Fig.7 shows a qualitative comparison of predictions using the models from Table 5. We note the clustering of false predictions in blocks for the upscaled output and the performance improvement at boundaries for the CSCL vs the randomly initialized model. Further comparisons using super-resolution training are included in the supplementary material.

5.5. Assessing the generality of CSCL pretraining

To assess the generality of our pretraining scheme we do further experiments in 2D and 3D image segmentation. For 2D experiments we use the *Cityscapes* [12] dataset because it includes multiple classes in the same image and thus it makes it possible for CSCL to generate negative pairs from a variety of semantic classes. For experiments in 3D image segmentation we use the *BRATS2020* dataset [26, 3, 2, 1] for brain tumor segmentation from multimodal MRI scans.

5.5.1 2D image semantic segmentation

We only use the fine annotated data from *Cityscapes*. This includes 2,979 and 500 images respectively in the *train* and *validation* sets. Each image is resized to 500×1000 pixels by means of bilinear interpolation. As a benchmark model we use a *FCN-ResNet50* with dilated convolutions in the two final blocks resulting in a final feature map of output stride 8 which is then bilinearly upsampled to match the input size. For all runs, including pretraining, we use the *SGD* optimizer with momentum 0.9 and initial learn rate 0.005, batch size 8 and a poly learn rate decay policy in which the initial learn rate is multiplied by $(1 - \frac{step}{total_steps})^{0.9}$ at every training step. Pretraining schedule uses $60k$ steps with parameters $w_d = 7$, $w_r = 4$, $w_s = 4$, $\lambda = 0.10$. Models are fine-tuned for $40k$ steps. Both networks are initialized with *ImageNet* pretrained weights. Results are presented in Table 6. We observe that the CSCL pretraining improves the final segmentation performance with no additional data.

5.5.2 3D volumetric image semantic segmentation

Here we are trying to predict one of four provided annotation types in *BRATS2020* brain tumor segmentation dataset.

model	mIoU
FCN-ResNet50	0.696
FCN-ResNet50-CSCL	0.712

Table 6: Model performance at *Cityscapes val* set. CSCL pretraining leads to improvements with no additional data.

A detailed description of the types of annotations can be found in [1]. All data were split into 339 scans for training and 30 scans for evaluation. To reduce the memory requirements we use $(64 \times 64 \times 64)$ and $(128 \times 128 \times 128)$ centered crops for pretraining and training which include all classes. For all experiments we use the *NVNet* model from [27] without the variational autoencoder branch. Training is performed with the *Adam* optimizer [24] with beta parameters (0.9, 0.999). The initial learn rate was set to 0.0005 (0.001 for pretraining) and learn rate decay 0.95 was applied every 5 epochs. We train with a batch size 2 for 500 epochs. For the CSCL pretraining we use a sliding window with $w_d = 3$, $w_r = 1$, $w_s = 1$, $\lambda = 0.05$. Results presented in Table 7 show macro metrics for the baseline and CSCL models. We note clear performance gains for the pretrained model for all metrics.

model	Acc.	mIoU	F1
NVNet	0.837	0.695	0.811
NVNET-CSCL	0.861	0.717	0.829

Table 7: Model performance on 3D *BRATS2020* MRI data. Improvement over the baseline method is obtained using no additional data.

6. Conclusion

In this study we tackled the problem of crop type semantic segmentation from satellite images. Motivated by an identified performance drop at object boundaries we proposed CSCL, a pretraining scheme targeting a CNN’s ability to model the relationship between each input location and its local neighborhood. Using our method we improved the state-of-the-art performance in crop type segmentation and showed its generality on semantic segmentation of 2D and 3D images. We believe this will be of interest to the broader computer vision community dealing with N-dimensional dense labelling tasks. Finally, we create a very large dataset for crop type semantic segmentation from satellite images which also enables training of semantic segmentation models at super-resolution. We make this data publicly available in an effort to facilitate further research into this domain.

References

- [1] Spyridon Bakas, Hamed Akbari, Aristeidis Sotiras, Michel Bilello, Martin Rozycki, Justin Kirby, John Freymann, Keyvan Farahani, and Christos Davatzikos. Advancing the cancer genome atlas glioma mri collections with expert segmentation labels and radiomic features. *Scientific Data*, 4, 09 2017. 8
- [2] Spyridon Bakas, Hamed Akbari, Aristeidis Sotiras, Michel Bilello, Martin Rozycki, Justin Kirby, John Freymann, Keyvan Farahani, and Christos Davatzikos. Segmentation labels and radiomic features for the pre-operative scans of the tcga-agg collection, 07 2017. 8
- [3] Spyridon Bakas, Mauricio Reyes, András Jakab, Stefan Bauer, Markus Rempfler, Alessandro Crimi, Russell Takeshi Shinohara, Christoph Berger, Sung Min Ha, Martin Rozycki, Marcel Prastawa, Esther Alberts, Jana Lipková, John B. Freymann, Justin S. Kirby, Michel Bilello, Hassan M. Fathallah-Shaykh, Roland Wiest, Jan Kirschke, Benedikt Wiestler, Rivka R. Colen, Aikaterini Kotrotsou, Pamela La-Montagne, Daniel S. Marcus, Mikhail Milchenko, Arash Nazeri, Marc-André Weber, Abhishek Mahajan, Ujjwal Baid, Dongjin Kwon, Manu Agarwal, Mahbubul Alam, Alberto Albiol, Antonio Albiol, Alex Varghese, Tran Anh Tuan, Tal Arbel, Aaron Avery, Pranjal B., Subhashis Banerjee, Thomas Batchelder, Kayhan N. Batmanghelich, Enzo Battistella, Martin Bendszus, Eze Benson, José Bernal, George Biros, Mariano Cabezas, Siddhartha Chandra, Yi-Ju Chang, and et al. Identifying the best machine learning algorithms for brain tumor segmentation, progression assessment, and overall survival prediction in the BRATS challenge. *CoRR*, abs/1811.02629, 2018. 8
- [4] I. Bello, B. Zoph, Q. Le, A. Vaswani, and J. Shlens. Attention augmented convolutional networks. In *2019 IEEE/CVF International Conference on Computer Vision (ICCV)*, pages 3285–3294, 2019. 3, 4
- [5] Jane Bromley, Isabelle Guyon, Yann LeCun, Eduard Säckinger, and Roopak Shah. Signature verification using a “siamese” time delay neural network. In *Proceedings of the 6th International Conference on Neural Information Processing Systems, NIPS’93*, page 737–744, San Francisco, CA, USA, 1993. Morgan Kaufmann Publishers Inc. 3
- [6] Ting Chen, Simon Kornblith, Mohammad Norouzi, and Geoffrey Hinton. A simple framework for contrastive learning of visual representations, 2020. 3
- [7] Xinlei Chen, Haoqi Fan, Ross Girshick, and Kaiming He. Improved baselines with momentum contrastive learning, 2020. 3
- [8] Sumit Chopra, Raia Hadsell, and Yann LeCun. Learning a similarity metric discriminatively, with application to face verification. In *Proc. of Computer Vision and Pattern Recognition Conference*. IEEE Press, 2005. 3
- [9] Özgün Çiçek, Ahmed Abdulkadir, Soeren S. Lienkamp, Thomas Brox, and Olaf Ronneberger. 3d u-net: Learning dense volumetric segmentation from sparse annotation. *CoRR*, abs/1606.06650, 2016. 3, 5
- [10] Christopher Conrad, Stefan Dech, Olena Dubovyk, Sebastian Fritsch, Doris Klein, Fabian Löw, Gunther Schorcht, and Julian Zeidler. Derivation of temporal windows for accurate crop discrimination in heterogeneous croplands of uzbekistan using multitemporal rapideye images. *Computers and Electronics in Agriculture*, 103:63–74, 2014. 2
- [11] Christopher Conrad, Sebastian Fritsch, Julian Zeidler, Gerd Rucker, and Stefan Dech. Per-field irrigated crop classification in arid central asia using spot and aster data. *Remote Sensing*, 2(4):1035–1056, 2010. 2
- [12] Marius Cordts, Mohamed Omran, Sebastian Ramos, Timo Rehfeld, Markus Enzweiler, Rodrigo Benenson, Uwe Franke, Stefan Roth, and Bernt Schiele. The cityscapes dataset for semantic urban scene understanding. In *Proc. of the IEEE Conference on Computer Vision and Pattern Recognition (CVPR)*, 2016. 8
- [13] Ovidiu Csillik and Mariana Belgiu. Cropland mapping from sentinel-2 time series data using object-based image analysis. 05 2017. 6
- [14] V. S. F. Garnot, L. Landrieu, S. Giordano, and N. Chehata. Time-space tradeoff in deep learning models for crop classification on satellite multi-spectral image time series. In *IGARSS 2019 - 2019 IEEE International Geoscience and Remote Sensing Symposium*, pages 6247–6250, 2019. 3
- [15] Vivien Sainte Fare Garnot, Loic Landrieu, Sebastien Giordano, and Nesrine Chehata. Satellite image time series classification with pixel-set encoders and temporal self-attention. In *Proceedings of the IEEE/CVF Conference on Computer Vision and Pattern Recognition (CVPR)*, June 2020. 2, 3, 5, 6
- [16] R. Hadsell, S. Chopra, and Y. LeCun. Dimensionality reduction by learning an invariant mapping. In *2006 IEEE Computer Society Conference on Computer Vision and Pattern Recognition (CVPR’06)*, volume 2, pages 1735–1742, 2006. 3, 4
- [17] Pengyu Hao, Yulin Zhan, Li Wang, Zheng Niu, and Muhammad Shakir. Feature selection of time series modis data for early crop classification using random forest: A case study in kansas, usa. *Remote Sensing*, 7(5):5347–5369, 2015. 2
- [18] Kaiming He, Haoqi Fan, Yuxin Wu, Saining Xie, and Ross Girshick. Momentum contrast for unsupervised visual representation learning. In *Proceedings of the IEEE/CVF Conference on Computer Vision and Pattern Recognition (CVPR)*, June 2020. 3
- [19] Roberto Interdonato, Dino Ienco, Raffaele Gaetano, and Kenji Ose. Duplo: A dual view point deep learning architecture for time series classification. *ISPRS Journal of Photogrammetry and Remote Sensing*, 149:91 – 104, 2019. 3
- [20] Xue Jinru and Baofeng Su. Significant remote sensing vegetation indices: A review of developments and applications. *Journal of Sensors*, 2017:1–17, 01 2017. 2
- [21] Yannis Kalantidis, Mert Bulent Sariyildiz, Noe Pion, Philippe Weinzaepfel, and Diane Larlus. Hard negative mixing for contrastive learning. In H. Larochelle, M. Ranzato, R. Hadsell, M. F. Balcan, and H. Lin, editors, *Advances in Neural Information Processing Systems*, volume 33, pages 21798–21809. Curran Associates, Inc., 2020. 4
- [22] Konstantinos Kamnitsas, Daniel Coelho de Castro, Loic Le Folgoc, Ian Walker, Ryutaro Tanno, Daniel Rueckert, Ben

- Glocker, Antonio Criminisi, and Aditya V. Nori. Semi-supervised learning via compact latent space clustering. In Jennifer G. Dy and Andreas Krause, editors, *Proceedings of the 35th International Conference on Machine Learning, ICML 2018, Stockholmsmässan, Stockholm, Sweden, July 10-15, 2018*, volume 80 of *Proceedings of Machine Learning Research*, pages 2464–2473. PMLR, 2018. 3
- [23] Prannay Khosla, Piotr Teterwak, Chen Wang, Aaron Sarna, Yonglong Tian, Phillip Isola, Aaron Maschiot, Ce Liu, and Dilip Krishnan. Supervised contrastive learning, 2020. 3
- [24] Diederik P. Kingma and Jimmy Ba. Adam: A method for stochastic optimization, 2014. cite arxiv:1412.6980Comment: Published as a conference paper at the 3rd International Conference for Learning Representations, San Diego, 2015. 6, 8
- [25] Kolya Malkin, Caleb Robinson, Le Hou, and Nebojsa Jojic. Label super-resolution networks. In *International Conference on Learning Representations*, 2019. 3
- [26] B. H. Menze, A. Jakab, S. Bauer, J. Kalpathy-Cramer, K. Farahani, J. Kirby, Y. Burren, N. Porz, J. Slotboom, R. Wiest, L. Lanczi, E. Gerstner, M. Weber, T. Arbel, B. B. Avants, N. Ayache, P. Buendia, D. L. Collins, N. Cordier, J. J. Corso, A. Criminisi, T. Das, H. Delingette, Ç. Demiralp, C. R. Durst, M. Dojat, S. Doyle, J. Festa, F. Forbes, E. Geremia, B. Glocker, P. Golland, X. Guo, A. Hamamci, K. M. Iftekharuddin, R. Jena, N. M. John, E. Konukoglu, D. Lashkari, J. A. Mariz, R. Meier, S. Pereira, D. Precup, S. J. Price, T. R. Raviv, S. M. S. Reza, M. Ryan, D. Sarikaya, L. Schwartz, H. Shin, J. Shotton, C. A. Silva, N. Sousa, N. K. Subbanna, G. Szekely, T. J. Taylor, O. M. Thomas, N. J. Tustison, G. Unal, F. Vasseur, M. Wintermark, D. H. Ye, L. Zhao, B. Zhao, D. Zikic, M. Prastawa, M. Reyes, and K. Van Leemput. The multimodal brain tumor image segmentation benchmark (brats). *IEEE Transactions on Medical Imaging*, 34(10):1993–2024, 2015. 8
- [27] Andriy Myronenko. 3d mri brain tumor segmentation using autoencoder regularization. In Alessandro Crimi, Spyridon Bakas, Hugo Kuijf, Farahani Keyvan, Mauricio Reyes, and Theo van Walsum, editors, *Brainlesion: Glioma, Multiple Sclerosis, Stroke and Traumatic Brain Injuries*, pages 311–320. Cham, 2019. Springer International Publishing. 8
- [28] Pedro O O. Pinheiro, Amjad Almahairi, Ryan Benmalek, Florian Golemo, and Aaron C Courville. Unsupervised learning of dense visual representations. In H. Larochelle, M. Ranzato, R. Hadsell, M. F. Balcan, and H. Lin, editors, *Advances in Neural Information Processing Systems*, volume 33, pages 4489–4500. Curran Associates, Inc., 2020. 3
- [29] Charlotte Pelletier, Silvia Valero, Jordi Inglada, Nicolas Champion, and Gérard Dedieu. Assessing the robustness of random forests to map land cover with high resolution satellite image time series over large areas. *Remote Sensing of Environment*, 187:156–168, 2016. 2
- [30] Charlotte Pelletier, Geoffrey I. Webb, and François Petitjean. Temporal convolutional neural network for the classification of satellite image time series. *Remote Sensing*, 11(5), 2019. 3
- [31] José M. Peña-Barragán, Moffatt K. Ngugi, Richard E. Plant, and Johan Six. Object-based crop identification using multiple vegetation indices, textural features and crop phenology. *Remote Sensing of Environment*, 115(6):1301–1316, 2011. 2
- [32] Prajit Ramachandran, Niki Parmar, Ashish Vaswani, Irwan Bello, Anselm Levskaya, and Jon Shlens. Stand-alone self-attention in vision models. In H. Wallach, H. Larochelle, A. Beygelzimer, F. d'Alché-Buc, E. Fox, and R. Garnett, editors, *Advances in Neural Information Processing Systems*, volume 32, pages 68–80. Curran Associates, Inc., 2019. 3, 4
- [33] Joshua David Robinson, Ching-Yao Chuang, Suvrit Sra, and Stefanie Jegelka. Contrastive learning with hard negative samples. In *International Conference on Learning Representations*, 2021. 4
- [34] Rose Rustowicz, Robin Cheong, Lijing Wang, Stefano Ermon, Marshall Burke, and David B. Lobell. Semantic segmentation of crop type in africa: A novel dataset and analysis of deep learning methods. In *CVPR Workshops*, 2019. 3, 5, 6
- [35] M. Rußwurm and M. Körner. Temporal vegetation modelling using long short-term memory networks for crop identification from medium-resolution multi-spectral satellite images. In *2017 IEEE Conference on Computer Vision and Pattern Recognition Workshops (CVPRW)*, pages 1496–1504, 2017. 3
- [36] Marc Rußwurm and Marco Körner. Multi-temporal land cover classification with sequential recurrent encoders. *ISPRS International Journal of Geo-Information*, 7(4):129, Mar 2018. 3, 5, 6
- [37] Marc Rußwurm, Charlotte Pelletier, M. Zollner, Sébastien Lefèvre, and Marco Körner. Breizhcrops: A time series dataset for crop type mapping. *ISPRS - International Archives of the Photogrammetry, Remote Sensing and Spatial Information Sciences*, XLIII-B2-2020:1545–1551, 08 2020. 3
- [38] Ruslan Salakhutdinov and Geoff Hinton. Learning a nonlinear embedding by preserving class neighbourhood structure. In Marina Meila and Xiaotong Shen, editors, *Proceedings of the Eleventh International Conference on Artificial Intelligence and Statistics*, volume 2 of *Proceedings of Machine Learning Research*, pages 412–419, San Juan, Puerto Rico, 21–24 Mar 2007. PMLR. 3
- [39] Xingjian SHI, Zhourong Chen, Hao Wang, Dit-Yan Yeung, Wai-kin Wong, and Wang-chun WOO. Convolutional lstm network: A machine learning approach for precipitation nowcasting. In C. Cortes, N. Lawrence, D. Lee, M. Sugiyama, and R. Garnett, editors, *Advances in Neural Information Processing Systems*, volume 28, pages 802–810. Curran Associates, Inc., 2015. 3
- [40] Sofia Siachalou, Giorgos Mallinis, and Maria Tsakiri-Strati. A hidden markov models approach for crop classification: Linking crop phenology to time series of multi-sensor remote sensing data. *Remote Sensing*, 7(4):3633–3650, 2015. 2
- [41] Joon Son Chung, Andrew Senior, Oriol Vinyals, and Andrew Senior. Lip reading sentences in the wild. In *Proceedings of the IEEE Conference on Computer Vision and Pattern Recognition (CVPR)*, July 2017. 3

- [42] Aäron van den Oord, Yazhe Li, and Oriol Vinyals. Representation learning with contrastive predictive coding. *CoRR*, abs/1807.03748, 2018. [3](#)
- [43] Ashish Vaswani, Noam Shazeer, Niki Parmar, Jakob Uszkoreit, Llion Jones, Aidan N Gomez, Łukasz Kaiser, and Illia Polosukhin. Attention is all you need. In I. Guyon, U. V. Luxburg, S. Bengio, H. Wallach, R. Fergus, S. Vishwanathan, and R. Garnett, editors, *Advances in Neural Information Processing Systems 30*, pages 5998–6008. Curran Associates, Inc., 2017. [3](#)
- [44] X. Wang, R. Girshick, A. Gupta, and K. He. Non-local neural networks. In *2018 IEEE/CVF Conference on Computer Vision and Pattern Recognition*, pages 7794–7803, 2018. [3](#)
- [45] Xinlong Wang, Rufeng Zhang, Chunhua Shen, Tao Kong, and Lei Li. Dense contrastive learning for self-supervised visual pre-training, 2020. [3](#)
- [46] Z. Wu, Y. Xiong, S. X. Yu, and D. Lin. Unsupervised feature learning via non-parametric instance discrimination. In *2018 IEEE/CVF Conference on Computer Vision and Pattern Recognition*, pages 3733–3742, 2018. [3](#)